Journal of the European Ceramic Society 45 (2025) 116963

Contents lists available at ScienceDirect

Journal of the European Ceramic Society

journal homepage: www.elsevier.com/locate/jeurceramsoc

Compositionally complex AlB_2-type diborides in dissociated air plasma

F. Monteverde [a,*], C. Pellegrini [b], M. Balat-Pichelin [b], W. Fahrenholtz [c], G. Hilmas [c]

[a] Institute of Science, Technology and Sustainability for Ceramics – National Research Council of Italy, Via Granarolo 64, Faenza I-48018, Italy
[b] PROMES-CNRS, UPR8521, 7 Rue Du Four Solaire, Font-Romeu Odeillo 66120, France
[c] Missouri University of Science and Technology, Rolla, MO 65409, United States

ARTICLE INFO

Keywords:
Compositionally complex diboride solid solution
Resistance to oxidation
Self healing
Air plasma
High temperature

ABSTRACT

Multi-metal compositionally complex (CC) AlB_2-type diboride solid solutions (SS) containing IV-V-VI group elements are garnering a steadily growing research interest. The present work explores the composition dependence of oxidation resistance on nominally equiatomic $(Hf,Me,Ta,Ti,Zr)B_2$ SS, Me = Nb or Cr, exposed to a dissociated air plasma (total pressure of about 1 kPa): specimens were exposed for 5 min at some selected set points between 1800 K and 2500 K using a solar furnace. The CC diboride with Nb showed superior resistance to oxidation compared to that with Cr. The experimental results showed good agreement with predictions based on a thermodynamic assessment.

1. Introduction

Desired future capabilities related to hypersonic flight [1], rocket propulsion [2], nuclear fusion [3], concentrated solar power and thermal energy storage [4] provide strong motivation in the search for new and better performing materials. These types of applications involve operating environments commonly defined as “extreme” due to temperatures, heat fluxes, chemical reactivities, radiation fluxes, and/or strain rates that are often beyond the capabilities of available materials.

In the 1990s and later, worldwide interest in hypersonic aviation increased [5]. This led to renewed interest in ultra-high-temperature ceramics (UHTCs), which has continued to flourish [6]. The definition of the main following acronyms is listed in Table 1. UHTCs have received considerable attention for their potential use in extreme environments based on properties including melting temperatures above 3300 K, strength retention above 2200 K, thermal conductivities of 100 W/(m·K) or higher, and thermochemical stability [7–10].

The so-called compositionally complex (CC) refractory ceramics are an emerging new class of multi-element materials. [6]’ [11,12] These ceramics are of great interest due to the potential to significantly expand the compositional breadth of UHTCs and the range of achievable properties. The most common nomenclature of this class of multi-element CC ceramics has been “high-entropy” ceramics [13] to acknowledge the gain in configurational entropy of mixing (ΔS^{C}_{mix}) obtained by alloying multiple metals onto a single-phase lattice. The ΔS^{C}_{mix} maximization approach was first applied to oxides [14] [15] and has thus been extended to other classes of ceramics including borides [16] and diborides [17,18], carbides [19–21], carbonitrides [22] or silicides [23].

While publications on the synthesis and densification of novel CC compositions are numerous [24,25], oxidation resistance studies remain sparse and have rarely addressed ranges of technological interest for temperatures above 2000 K. Ni et al., exposed high-entropy carbides to an oxyacetylene torch at 2273 K [26]. Characterization at multi-length scales revealed the formation of compositionally complex oxide sub-layers. Wang et al. tested the (Hf,Nb,Ta,Zr)C and pushed the test temperature up to 2373 K using a plasma flame gun in air: oxide layers with complex compositions formed an effective barrier against ablation [27]. Finally, Li et al., tested a novel $(Hf_{1/3}Zr_{1/3}Ti_{1/3})C$ carbide coating with excellent long-life ablation resistance above 2373 K [28]

As for CC diborides, most AlB_2-type SSs showed lower weight gains than individual diboride ceramics produced with the same processing conditions [13]. For example, $(Hf,Mo,Nb,Ta,Ti)B_2$ ceramics exhibited low and stable oxidation rates up to 1473 K, whereas TiB_2 and TaB_2 had significant weight gains below 1000 K. Wen et al., first fabricated CC $(Hf,Sm,Ta,Zr)B_2$ with 0–25 mol% Sm contents via a two-step technology and then studied their oxidation resistance in the range 1473–1773 K [29]. Feltrin et al., studied the high temperature oxidation kinetics at 1773 K of a metastable dual-phase diboride (DPB) and a high-entropy diboride (HEB) [30]. Both ceramics displayed linear oxidation behaviour but the oxidation rate of the DPB was found to be 2.8 times higher than that of the HEB. Bin Hoque et al., studied thermal and ablation properties of a $(Hf_{0.2}Nb_{0.2}Ti_{0.2}Ta_{0.2}Zr_{0.2})B_2$ solid solution [31]: they

* Corresponding author.
E-mail address: frederic.monteverde@issmc.cnr.it (F. Monteverde).

https://doi.org/10.1016/j.jeurceramsoc.2024.116963
Received 4 July 2024; Received in revised form 16 September 2024; Accepted 1 October 2024
Available online 2 October 2024

Table 1
List of most common acronyms used in the main text.

CC	Compositionally complex	HSC	Equilibria computing package
CCB	Compositionally diboride	MESOX	Moyenne d'Essai Solaire d'oxydation
DFB	Dual phase diboride	PRDP	Partially reacted diboride powder
EDS	Energy dispersive spectroscopy	SPS	Spark plasma sintering
ED-XRF	Energy dispersive x-ray fluorescence	SS	Solid solution
FESEM	Field emission scanning electron microscope	UHTC	Ultra-high temperature ceramics
HEB	High entropy diborides	XRD	X-ray diffraction

concluded that such CC diboride solid solutions were suitable for high thermal loads in extreme environments. To the best of the authors' knowledge, the most comprehensive work on oxidation resistance of CC diborides published to date was by Backman et al., [32–35]. Both analytical and computational thermodynamic approaches were used to investigate the oxidation behavior of (Hf,Nb,Ta,Ti,Zr,)B_2, which was the focus of recent research campaigns. [13,17,18,24]. Ye et al., added insights on the design and optimization of multi-component UHTCs by elucidating the role of the active oxidation of some species during ablation [36].

The present work explores the composition dependence of the oxidation resistance in dissociated air plasma on two nominally equiatomic (Hf,Me,Ta,Ti,Zr)B_2 SSs, Me=Cr or Nb, exposed to up to 2500 K in dissociated air plasma.

2. Experimental methods

2.1. Materials: fabrication and characterization

Two compositionally complex diboride (CCB) compositions were tested, which are designated as follows:

CCB-Nb: (Hf, **Nb**, Ta, Ti, Zr)B_2

CCB-Cr: (**Cr**, Hf, Ta, Ti, Zr)B_2

Partially reacted diboride powders (PRDPs) were synthesized at 1923 K by a boro/carbothermal reduction process of metal oxide mixtures and using B_4C and C as reducing agents. Densification of PRDPs was accomplished at 2273 K for CCB-Cr or 2373 K for CCB-Nb by spark plasma sintering (SPS, DCS10, Thermal Technology) under mild vacuum (~2 Pa), an applied uniaxial pressure of 50 MPa, and a final isothermal holding time of 10 min. The SPS furnace was cooled to 1273 K at 50 K/min and under a uniaxial pressure of 25 MPa and then cooled at the natural furnace rate to room temperature. More details of the synthesis and densification are reported elsewhere [37]. For each composition, five sintered pellets were fabricated that had a diameter of 20 mm and thickness of about 2 mm. Both sides of each pellet were ground to remove the graphite foil and any reaction layers. For electron microscopy and chemical analyses of the as-sintered materials, pellets were polished to a 1 μm finish using diamond suspensions; the last step was a finishing treatment using a colloidal silica suspension (about 50 nm average particle size). Microstructures of the as-sintered materials were analysed using field emission scanning electron microscopy (FESEM, ZEISS ∑igma – Germany). In-situ chemical analysis and elemental maps by energy dispersive spectroscopy (EDS, INCA Energy 300 , Oxford Instruments – UK) were acquired on the as-produced materials. The accelerating voltage was generally set to 20 keV. Phase compositions of the as-sintered materials were determined by laboratory X-ray diffractometer (XRD, D8 Advance, Bruker - Germany), using Ni filtered Cu Kα radiation. A parallel quantitative determination of the overall metal concentration in the as-sintered specimens was also accomplished using an energy dispersive X-ray fluorescence spectrometer (ED-XRF, S2 PUMA, Bruker) on one 20 mm diameter surface of an as-sintered disc. The bulk density (ρ_B) of each as-produced pellet was measured by Archimedes' method using distilled water as the immersing medium.

2.2. Resistance to oxidation: experimental device, test, and characterization

The resistance to oxidation of CCB-Nb and CCB-Cr was tested using the Moyen d'Essai Solaire d'Oxydation (MESOX) reactor placed at the focus of the 6 kW Odeillo solar furnace [38]: a general schematic of the plant is shown in Fig. SI-1. The experimental parameters were selected to partially reproduce atmospheric re-entry to Earth. The total pressure inside the reactor was set to about 1 kPa, representing the atmospheric pressure in between 80 and 60 km altitude where the dissociation of oxygen occurs due to the speed of the re-entry vehicle. The surface temperature of the specimens was measured using a monochromatic optical pyrometer that operated at a wavelength of 5 μm. The temperature range of interest was about 1800 K to 2500 K. Other details about the MESOX reactor are reported in the supplementary information file (SI).

Upon cooling, an analytical balance (±0.1 mg of instrumental accuracy) determined the post-test mass. The mass change (Δm) of each pellet was normalized to the exposed surface area (S) which has a diameter of 20 mm plus the external cylindrical walls of the pellet. The as-exposed front surface of each pellet was analyzed by ED-XRF, XRD and FESEM-EDS. For ED-XRF, the collected signals came from the entire exposed surface. For XRD, data were collected on a 15-mm long strip inside the exposed area.

Prior to sectioning, each pellet was embedded in resin to preserve the integrity of the external oxide layers during cutting and polishing. Specimens were cut into two half-moon-shaped pieces using a 0.5 mm thick diamond blade. The diametral cut allows for analysis of the geometrical center of the pellet, which was the approximate point at which the optical pyrometer was focused. The cross-sections remained in the original resin and were further embedded in a conductive resin, polished according to the method described above, and then analyzed by FESEM-EDS. A carbon coating that was a few nm thick was sputtered onto the polished surfaces to minimize charging during SEM analysis. Elemental mapping of selected areas of the oxide layers was done by FESEM-EDS. An 3D optical microscope (HIROX mod. RH-2000) was used to observe the polished diametral cuts and provide a representative thickness range of the external scale altered by oxidation.

3. Thermodynamic assessment

Equilibrium vapor pressures of volatile species ($p_{vap,i}$) were computed as a function of temperature (T) for the most stable solid compounds using the commercial package HSC Chemistry v.6.12 [39]. Table 2 defines some of the nomenclature used in the main text.

The CCBs were modeled as non-interacting ideal phases of the

Table 2
Main nomenclature used in the main text.

Category	Symbol	Unit	Description
Constant	R	J mol^{-1} K^{-1}	Universal constant of gases
	p_0	Pa	Operating pressure inside the quartz tube
Subscript	vap		Volatilization process
	i		Relative to a volatile species "i"
Superscript	Me		Me(g) and Me-O (g) volatile species are considered
	MeO_2		Only MeO_2(g) is considered
Variable	p	Pa	Pressure
	p_{O2}	Pa	Oxygen partial pressure
	j	g m^{-2} s^{-1}	Mass flux volatilization
	T	K	temperature
	Q	-	Dimensionless tendency-to-volatilize
	hi	W m^{-2}	heat flux
	M	g mol^{-1}	molar mass

separate equimolar MeB_2 compounds, each had unit activity when reacting with oxygen. Some assumptions were made: i) p_0 was set equal to 1 kPa; ii) the oxygen partial pressure (p_{O2}) was varied from 200 Pa down to 1 Pa with Ar as an inert component added to keep p_0 constant; iii) the solid/liquid oxides in the database are MeO_x (s,l). The lack of available thermodynamic data for ternary and more complex solid compounds and solid solutions limits the ability to include phases actually present in the specimens during analysis. The values of $p_{vap,i}$ versus T were computed by HSC [39] and were used to describe the tendency of various volatile Me-containing oxides to volatilize from the solid. Eq. (1) was adopted to describe the tendency-to-volatilize for each component of the CCBs.

$$j_{vap,i} = p_{vap,i}\left(\frac{M_i}{2\pi RT}\right)^{1/2} \quad (1)$$

Eq. (1), known as the Hertz-Knudsen-Langmuir relation [36,40–42], describes the worst case of evaporation, i.e., the maximum possible mass flux volatilization when: 1) the evaporation from a free surface occurs at low p_0; and 2) re-condensation is ignored. Under these assumptions, a new useful descriptor was defined as follows:

$$Q^{Me} = \frac{j_{tot}^{Me}}{j_{vap}^{MeO_2}} \quad (2)$$

where

$$j_{tot}^{Me} = \sum_{i=1}^{no} j_{vap,i}^{Me} \quad (3)$$

to evaluate the tendency-to-volatilize of a metal (Me) and its volatile oxides (see Table 3). Given a specific MeB_2, each $p_{vap,i}$ value was calculated for all thermodynamically predicted volatile oxide products for reactions with oxygen at specific temperatures. The $p_{vap,i}$ values were converted into $j_{vap,i}$ using Eq. (1) and finally summed using relation (3). To dampen the bias to compare j_{tot}^{Me} values affected by dissimilar molar masses, Mi, the rescaling factor $j_{vap}^{MeO_2}$ was applied to normalize the Q^{Me} data calculated at a certain T and p_0. In fact, for a given Me, $j_{vap}^{MeO_2}$ is the mass flux volatilization occurring when 1 mol of MeB_2 is fully converted to gaseous products according to reaction (4)

$$MeB_2\ (s) + 5/2\ O_2\ (g) = MeO_2(g) + B_2O_3\ (g) \quad (4)$$

In other words, at a certain temperature and pressure, for a given MeB_2, when j_{tot}^{Me} tends to j_{vap}^{MeO2} it is assumed that the *in-situ* formed solid/liquid metal oxides are completely lost from the external surface.

The values for Q^{Me} can vary over several orders of magnitude depending on T and the limited ability of various metal-containing oxides to form stable solid phases due to excessive $p_{vap,i}$ compared to p_0.

Fig. 1 shows the Q^{Me} values when considering all Me-O species listed in Table 3 for the temperature range of 1800 K to 2600 K and p_{O2} = 200 Pa. Based on Fig. 1, the most stable oxides present at the surface are expected be composed of Hf, Zr or a mix of the two based on having the lowest Q^{Me} values. For example, at 2400 K Q^{Hf} is 4 $\times 10^{-5}$ % and Q^{Zr} is 9 $\times 10^{-4}$ %, while at the same T Q^{Ti} was 7.6 %, Q^{Ta} was 12.5 %, Q^{Nb} was 74.9 %, and Q^{Cr} reached 90.1 %. Other metals like Mo, W and V also have higher Q^{Me} values compared to Hf and Zr and, therefore, lower probabilities of forming stable solid oxide phases. Q^{Me} values (Me= Mo, W, and V) were plotted separately because their ranges were lower than Q^{Hf} or Q^{Zr}: for example, Q^{W} was 51.2 %, Q^{Mo} was 91.3 %, and Q^{V} reached 97.6 %. For comparison, the values of Q^{Si} were also calculated for SiC, an important refractory structural ceramic, considering reaction (5)

$$SiC\ (s) + 3/2\ O_2\ (g) = SiO_2(g) + CO\ (g) \quad (5)$$

to set the $j_{vap}^{SiO_2}$ reference value. Compared to IV group metal oxides, Si stands a poor chance of surviving at the surface as a Si-containing oxide, especially for T > 2400 K with Q^{Si} reaching a value of 44.8 %.

The oxygen partial pressure (p_{O2}) was varied from 200 Pa to 1 Pa to better elucidate its role in oxide stability. Fig. 2 summarizes the total vapor pressure p_{vap}^{Me} versus T calculated according to Eq. (6)

$$p_{vap}^{Me} = \sum_{i=1}^{no} p_{vap,i} \quad (6)$$

for the six metals used in the two current CCB compositions, and setting p_{O2}= 200 Pa or p_{O2} = 1 Pa. The value of 200 Pa is the p_{O2} in the air plasma while the p_{O2} value of 1 Pa was selected arbitrarily as representative of the low(er) p_{O2} at the innermost oxide/oxide interfaces. Hf and Zr are less volatile at p_{O2}= 200 Pa, while Cr is the most volatile at p_{O2} = 200 Pa followed by Nb, while at p_{O2}= 1 Pa the most volatile remains Cr followed by Ti. The p_{vap}^{Me} gradients can be used to describe compositions of species at different points in the oxide scale: for instance, the behaviour of p_{vap}^{Ti} gradients may produce zones of depletion. Data plotted in Fig. 2 confirm the tendency of Hf and Zr to form more stable solid oxides based on partial pressures that were up to 4 orders of magnitude lower than the other oxides. At the same time, the computed outputs indicate that Nb, Ta and Cr are more prone to volatilize from surfaces exposed to high temperatures due to higher vapor pressures. To summarize, the calculations predict that the IV group transitional metals Zr and Hf preferentially oxidize over the V-VI group metals, while the substrate (where p_{O2} is expected be lower than the exterior) can be enriched in V group elements. The extent of oxidation of the different metals also corresponds to their oxide thermodynamic favorability. Hf and Zr, which form the most stable oxides, oxidize preferentially, followed by Ti. Of the V group elements, Ta_2O_5 is more stable than Nb_2O_5, and thus Ta is expected to preferentially oxidize over Nb. Finally, the VI group elements, such as Cr, is predicted to volatilize, without the possibility to be effectively retained in some ordered form at the outermost external surface or at some innermost interfaces.

Table 3
Number (n_0) of volatile metal-carrying species available in the HSC package [39] and used to calculate formula (3).

Metal	Group	n_0	*Me (g)*	*Me-O(g)*
Hf	IV	3	Hf	HfO, HfO_2
Zr	IV	3	Zr	ZrO, ZrO_2
Ti	IV	3	Ti	TiO, TiO_2
Ta	V	3	Ta	TaO, TaO_2
Nb	V	3	Nb	NbO, NbO_2
V	V	3	V	VO, VO_2
Cr	VI	4	Cr	CrO, CrO_2, CrO_3
Mo	VI	7	Mo	MoO, MoO_2, MoO_3, $(MoO_3)_2$, $(MoO_3)_3$, $(MoO_3)_4$
W	VI	8	W	WO, WO_2, WO_3, W_3O_8, $(WO_3)_2$, $(WO_3)_3$, $(WO_3)_4$
Si		3	Si	SiO, SiO_2

4. Results

4.1. Characterization of baseline materials

The main data of the microstructure characterization of the two baseline CCBs are reported in Table 4. The average bulk densities (ρ_B) slightly differ from the theoretical density values previously measured and reported in reference 37.

Some residual boron carbide inclusions with diameters of up to several tens of microns were observed by SEM, as shown in Fig. 3.

For each composition, XRD analysis identified only one crystalline compound, which was indexed as an AlB_2-type phase with the space group P6/mmm. The residual boron carbide was not detected by XRD. Elemental chemical analysis by ED-XRF showed that the constituent

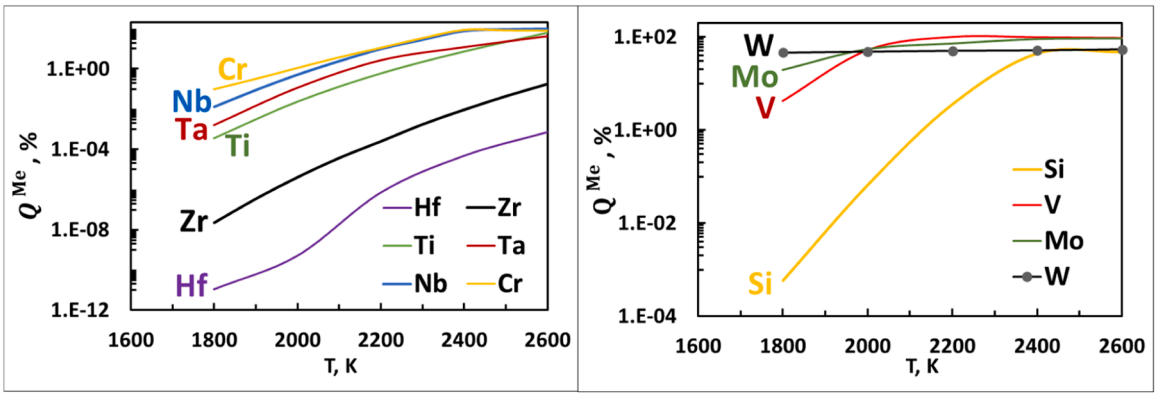

Fig. 1. Tendency-to-volatilize Q^{Me} versus temperature (T), p_0= 1 kPa and p_{O2}= 200 Pa.

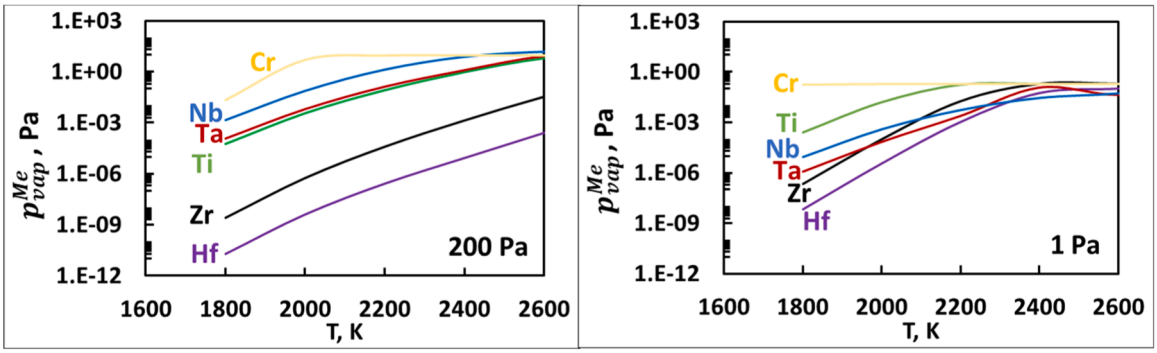

Fig. 2. Total vapor pressure p^{Me}_{vap} versus temperature (T) of the Me-carrying volatile products of Table 3: pO_2 = 200 or 1 Pa, respectively, rebuilds conditions at the exterior or at some innermost oxide/oxide interfaces.

Table 4
Peak temperature (T_{MAX}) during final 10 min dwell, expected density (ρ_{EXP}), bulk density (ρ_B) and their ratio, residual volume of the unreacted B_4C, final relative density (rd_F) accounting for residual B_4C, and (calculated) residual porosity (rp).

Sample	T_{MAX}	*ρ_{EXP} (± 0.01)	ρ_B (± 0.1)	ρ_B/ ρ_{EXP}	B_4C (± 0.2)	rd_F	rp**
	K	g/cm^3	g/cm^3	%	vol%	%	%
CCB-Cr	2273	7.93	7.6	95.8	6.5	99.7	0.3
CCB-Nb	2372	8.20	7.9	96.3	6.0	99.5	0.5

(*) [37]; (**) rp = 1-rd_F;

metals were present in nearly equiatomic amounts (i.e., 20 at% on a metals basis) in both CCBs. FESEM-EDS confirmed the atomic amounts (see Table 5) and was able to show that the long-range distribution was homogeneous among the different grains. Apart from the residual boron carbide, the analysis derived from ED-XRF, FESEM-EDS, and XRD showed that the baseline materials were single phase and that the matrices of CCB-Nb and CCB-Cr were nearly equimolar (Me,Ta,Ti, Zr,Hf) B_2 solid solutions, Me= Nb or Cr.

The AlB_2-type single phase CCBs were assumed to be stoichiometric, i.e, having a boron-to-metal ratio equal to 2 based on the narrow stoichiometry of the individual MeB_2 compounds. The relative density ratios based on the expected theoretical densities were 95.8 % for CCB-Cr and 96.3 % for CCB-Nb, which were below 100 % because of the residual volume of unreacted B_4C present in the final ceramics. [36] Image analysis of SEM micrographs was used to estimate the volume occupied by the unreacted boron carbide, as shown in Table 4. The final relative densities (rd_F) were corrected for the B_4C content using a linear volumetric rule-of-mixtures and assuming a theoretical density of 2.52 g/cm^3 for B_4C. This enabled the residual porosity (p) to be estimated using the calculation rp= 1- rd_F. Based on the density measurements and SEM analysis, the final CCBs were nearly fully dense.

4.2. During exposure to dissociated air plasma

The pellets (20 mm diameter) were exposed to increasingly severe concentrated solar fluxes (h_i) by controlling the opening of the shutter placed between the solar concentrator and the pellet (see Fig. SI-1). Table 6 shows the pertinent experimental details and results of the exposures. The highest h_i was 5.2 MW/m^2 and was used for pellets CCB-Nb-E and CCB-Cr-E. Fig. 4 shows the surface temperature (T_H) versus time for CCB-Nb and CCB-Cr discs at the maximum h_i. The solar shutter was fully opened for 300 s. The specimens reached their maximum T after lag times of about 180 s (CCB-Nb-E) and 130 s (CCB-Cr-E). Average values $<T_H>$ and related variability (ΔT_H) are reported in Table 6 for all the tests. The experimental temperature variability (ΔT_H) reported in Table 6 is based on fluctuations recorded during testing. The shutter opening was adjusted to heat pellets of both compositions to similar $<T_H>$ ranges for comparison. Moreover, except CCB-Nb-A, the ratio r= $(\Delta T)_H/<T_H>$ never exceeded 1 %.

In the case of CCB-Nb-E and CCB-Cr-E that were both exposed to the fully available concentrated solar flux of 5.2 MW/m^2, CCB-Nb-E reached an average radiative equilibrium temperature of 2525 K, about 150 K higher than CCB-Cr-E which was 2375 K. The values of the ratio "r" reported in Table 6 show that, during the 5-min exposure (at constant h_i= 5.2 MW/m^2), the surface temperature T of the zone impinged by the concentrated solar flux remained nearly constant. All specimens underwent rapid cooling when the shutter was closed. CCB-Cr-E failed during cooling. In addition, a greenish deposit formed on the internal walls of the quartz tube, which may have affected the concentrated solar

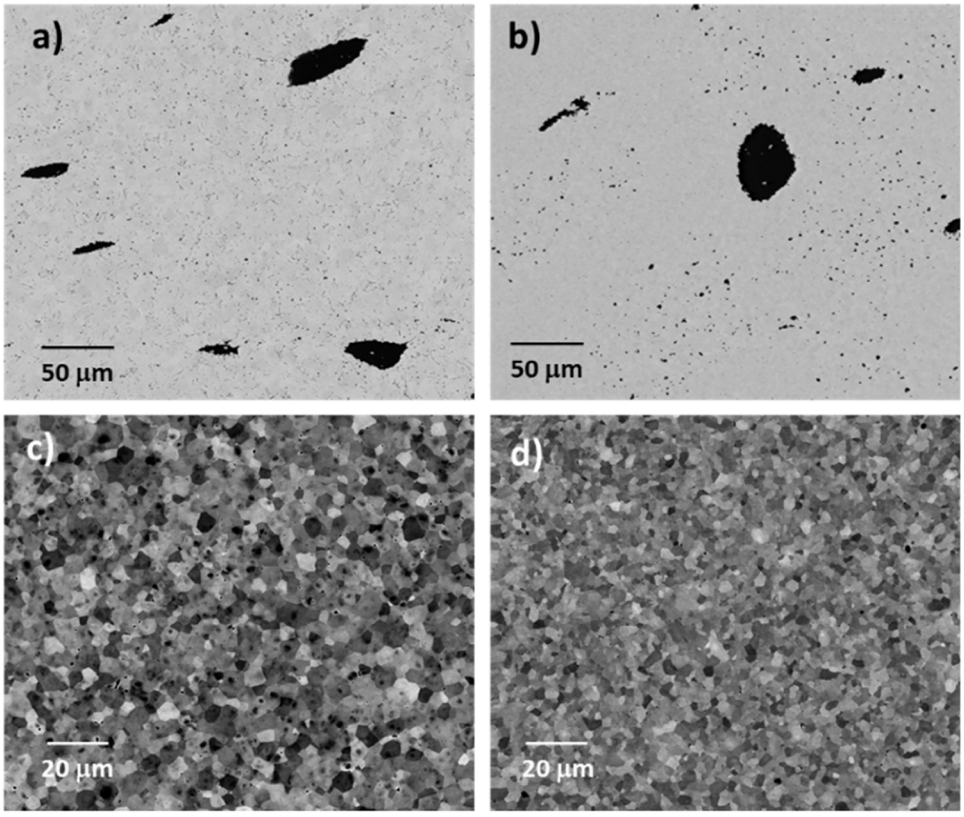

Fig. 3. Back-scattered electrons FESEM images (polished section) from the as-sintered CCB-Nb (a, c) and CCB-Cr (b, d). Panels a-b) primarily emphasize residual discrete boron carbide (dark) islands, panels c-d) provide an overview of the base microstructure.

Table 5
Experimental atomic average compositions (at%, metal basis) as determined by ED-XRF (within 0.1 % error) from the disc surface of 3.14 cm^2, and from the average of at least three areas of 10^{-2} mm^2.

	Cr		Hf		Nb		Ta		Ti		Zr		W	
CCB-	XRF	EDS	XRF	EDS	XRF	EDS	XRF	EDS	XRF	EDS	XRF	EDS	XRF	EDS
Cr	19.4	19.3	19.2	19.5	-	-	20.6	20.2	19.1	19.6	20.8	20.4	0.9	1.0
Nb	-	-	19.6	20.0	19.5	19.1	20.4	20.1	19.3	20.1	20.4	20.0	0.8	0.7

Table 6
Sample name with test label, average $<T_H>$ and variability $(\Delta T)_H$ of the surface temperature during the 5-min isothermal hold, assigned group number 1 or 2 based on $<T_H>$ range below/above 2270 K, ratio $r = (\Delta T)_H / <T_H>$, specific mass change (ΔM/S), concentrated solar flux (h_i) and thickness range of the oxide scale (Δd).

Test label	$<T_H> \pm (\Delta T)_H$	Group number	r	ΔM/S ± 0.02	h_i	Δd
CCB-x-y	(K)		%	(mg/cm^2)	MW/m^2	µm
Nb-A	1835 ± 29	**1**	1.58	1.30	n/a	80–90
Nb-B	2045 ± 13	**1**	0.64	2.90	n/a	100–110
Nb-C	2215 ± 12	**1**	0.54	0.80	n/a	50–60
Nb-D	2300 ± 9	2	0.39	2.20	n/a	50–55
Nb-E	2525 ± 12	2	0.48	1.30	5.2	80–100
Cr-A	1875 ± 16	**1**	0.85	−0.60	n/a	40–45
Cr-B	2115 ± 10	**1**	0.47	1.00	n/a	70–80
Cr-C	2180 ± 11	**1**	0.50	−0.40	n/a	70–80
Cr-D	2275 ± 12	2	0.53	−0.60	n/a	85–95
Cr-E	2375 ± 16	2	0.67	−3.10	5.2	80–85

n/a: not determined;

flux impinging the CCB-Cr-E during experiment and, therefore, the maximum surface temperature that was reached during exposure.

4.3. After exposure to dissociated air plasma

Overall integrity and visual appearance of some discs after exposure are displayed as inset in Fig. 4, while the complete series is displayed in Figs. SI-2–1/SI-2–2. In fact, the visual appearance of the exposed surfaces changed as soon as the heat flux h_i was gradually increased and reached the highest value of 5.2 MW/m^2 during the test of CCB-Nb-E and CCB-Cr-E. The prevailing yellowish (CCB-Nb-A) or whitish (CCB-Cr-A) surface coloration indicated that an external scale had formed. In addition, the external scale in CCB-Cr-A was less adherent than in CCB-Nb-A. The irregular dark areas visible in CCB-Nb-A and CCB-Cr-A came from partial detachment of the outer scale fragments during handling of the sample upon cooling. Although CCB-Nb-A and CCB-Cr-A were subjected to similar heating, and their bright visual coloration seemed similar, the chemical compositions of the as formed external scales were actually significantly different as described below. The crystalline phases present on the outer oxide layers were diverse: the possible alternate phases are listed in Table 7 while the complete summary of all the matching phases found are reported in Table 8. The assignment of crystalline phases with structures tabulated in the ICDD database is an

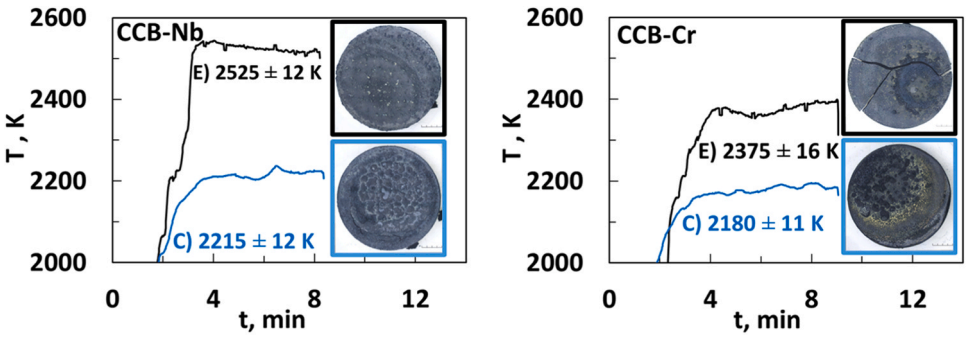

Fig. 4. Measured surface temperature (T) versus time (t) of some CCB discs: average temperature $<T_H>$ and variability ΔT_H during the 5-min isothermal hold as well as their post-test visual appearance are shown. CCB-Cr-E failed during cooling.

Table 7
Indicated phase, crystal system, possible alternate phase, PDF number or references, and label used are indicated.

Indicated phase	Crystal system	Possible alternate phase	Reference	Label	Match found in
ZrO_2, HfO_2	Monoclinic	$(Hf,Zr)O_2$	06–0318, 37–1484	P−1	Nb-C, Nb-D, Nb-E Cr-C, Cr-D, Cr-E
ZrO_2, HfO_2	Tetragonal	$(Hf,Zr)O_2$	48–0224	P−2	Nb-C, Nb-D Cr-C, Cr-D, Cr-E
$Zr_6Nb_2O_{17}$	Orthorhomic	$(Zr,Hf)_6(Ta,Nb)_2O_{17}$	09–0251	P−3	Nb-B, Nb-C Cr-A, Cr-B, Cr-C
Ta_2O_5	Orthorhombic	Ta_2O_5	25–0922	P−4	Nb-B, Cr-B*
$HfTiO_4$	Monoclinic	$(Zr,Hf)TiO_4$	31–0573	P−5	Nb-A
$HfTiO_4$	Orthorhombic	$(Zr,Hf)TiO_4$	40–0794	P−6	Nb-A
Cr_2O_3	Rhombohedral	Cr_2O_3	38–1479	P−7	Cr-A
TiO_2	Tetragonal	TiO_2	21–1276	P−8	Nb-B, Cr-A
$TiTa_2O_7$	Monoclinic	$Ti(Ta,Nb)_2O_7$	21–1424	P−9	-
ZrO_2	Orthorhombic	$(Zr,Ti)O_2$	35–0584	P−10	-
Ti_2ZrO_6	Orthorhombic	$Ti_2(Zr,Hf)O_6$	46–1265	P−11	-
$Nb_4Ta_2O_{15}$	Tetragonal	$Nb_4Ta_2O_{15}$	15–0114	P−12	-
$Ti_2Nb_{10}O_{29}$	Monoclinic	$Ti_2(Nb,Ta)_{10}O_{29}$	13–0317	P−13	-

(*) uncertain

indication of the structures that formed rather than the actual chemical compositions, which is why possible alternate phases are also listed in Table 7.

XRD analyses confirm that the microstructure evolution depends on $<T_H>$ (see Table 5). Added to this is the additional difficulty of multiple overlapping peaks for the possible alternate phases whose composition can evolve versus $<T_H>$ that ultimately make the assignment of XRD peaks rather challenging. In any case, some reliable assignments were made as shown in Table 8. The XRD patterns and the relative assignment of CCB-Nb-C, CCB-Cr-C, CCB-Nb-E and CCB-Cr-E were plotted in Fig. 5 as representative of group nr. 1 and nr. 2. For CCB-Nb-A, where $<T_H>$ remained below 2000 K, the mixed oxides P5 and P6 were present. Increasing $<T_H>$ to 2045 K, resulted in a more complex oxide layer on CCB-Nb-B that contained a mixed $(Hf,Zr)_6(Ta,Nb)_2O_{17}$ -like oxide labelled P3, together with P4 and a minor amount of titanium oxide P8. Increasing $<T_H>$ to 2215 K, the P3 mixed oxide was still present, together with other mixed oxides labelled P1 and P2 having, respectively, monoclinic and tetragonal structures like zirconia or hafnia. The mixed oxide P2 almost disappeared when $<T_H>$ reached 2525 K, and the mixed oxide P1 dominated the as-formed surface crystalline structure. The cell parameters of the monoclinic P1 phase in CCB-Nb-E were a=5.2906(14) Å, b= 5.1634(13) Å, b= 5.1634(13) Å, 5.1092(13) Å, β= 99.24(14) degrees. These results are in good agreement with the data of McCormack et al. [43] and of Liu et al., [44] which, respectively, gave a maximum stability temperature lower than 2800 K for $Hf_6Ta_2O_{17}$ and 2220 K for $Zr_6Ta_2O_{17}$. Part of the possible alternate phases listed in Table 7, such as P9-P10-P11-P12-P13, was retrieved from published data but no apparent match with our experimental data was found.

For the CCB-Cr pellets exposed at $<T_H>$ of about 1875 K, a Cr_2O_3 -like structure labelled P7 was detected together with a minor amount of titanium oxide P8 and the mixed $(Hf,Zr)_6Ta_2O_{17}$ like phase labelled P3. Increasing $<T_H>$ from 2115 K up to 2180 K caused P4 to disappear, the P1 and P5 phases to appear and the P3 phase to become the dominant phase. At the highest $<T_H>$ of 2375 K, the mixed oxides P1 and P2 were present on the surface while P3 was not stable anymore at these conditions according to Liu et al. [44].

The ED-XRF chemical analyses shown in Fig. 6 determined the amount of each metal on the as-oxidized surfaces in the areas heated by the solar probe. FESEM-EDS chemical analyses were conducted in parallel and were consistent with the outputs obtained using ED-XRF. The starting substrates contained a near equiatomic mixture of the metals (see Table 5), so larger deviation of one or more metals percentage from equiatomicity can be attributed the formation of stable solid oxides compared to volatile ones. In the case of CCB-Nb-E, for instance, besides a minor amount of P2 tetragonal phase, the remaining XRD peaks can be indexed according to the $(Hf,Zr)O_2$ like P1 monoclinic phase. Such a determination matches well with the related ED-XRF analysis in Fig. 6 which clarifies that the amount of Zr+Hf (at%, metal basis) of the metals present in P1 is 70.9 % while Ta/Ti/Nb are, respectively 11.3 %/

Table 8
Summary of the matching phases found in the XRD patterns: the corresponding $<T_H>$ value for each specimen is shown.

CCB-, group nr. 1						CCB-, group nr. 2			
Nb-A	Cr-A	Nb-B	Cr-B	Nb-C	Cr-C	Nb-D	Cr-D	Nb-E	Cr-E
1835 K	1875 K	2045 K	2115 K	2215 K	2180 K	2300 K	2275 K	2525 K	2375 K
P5, P6	P3, P7 P8	P3, P4 P8	P3, P4*	P1, P3, P4, P5, P8	P1, P3 P5	P1 P2	P1 P2	P1 P2	P1 P2

(*) uncertain

Table 9
Values of some known eutectic temperature (in K) between metal oxides pairs. Separate metal oxides are listed by periodic group.

Eutectic, K		IV			V		VI
		HfO_2	ZrO_2	TiO_2	Nb_2O_5	Ta_2O_5	Cr_2O_3
IV	HfO_2	**3173**					
	ZrO_2	2990	**2950**				
	TiO_2	2015	2120	**2130**			
V	Nb_2O_5	n/a	1710	1750	**1785**		
	Ta_2O_5	2005	1965	1895	1800	**2145**	n/a
VI	Cr_2O_3	n/a	2300	n/a			**2540**

n/a: not available; the melting point of the pure compound is underlined.

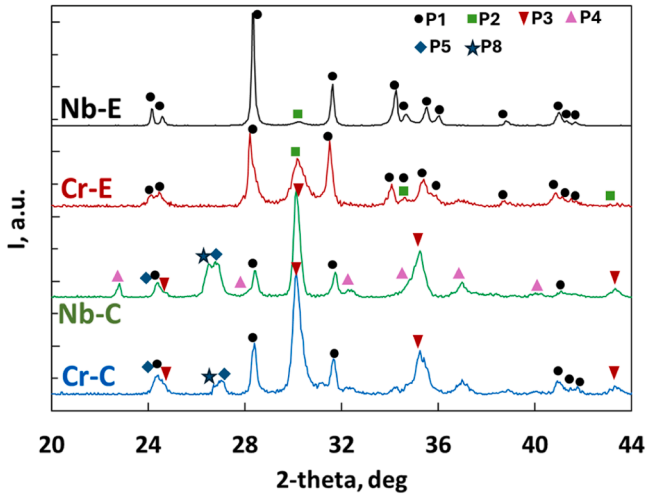

Fig. 5. X-ray diffraction patterns taken after oxidation in dissociated air exposed for 5 min at a certain average temperature <T_H>. The candidate structure-label correspondence is reported in Table 7.

10.2 %/7.5 %. The plots show that Hf-Zr based oxides are the most abundant species with increasing <T_H> and that Nb+Ta, or Cr+Ta are lost preferentially. The behavior of Ti fell outside the others in that it resisted volatilization, but FESEM-EDS analyses indicated that a Ti depletion zone could form in CCB-Nb.

To gain deeper insight into the effects of the oxidation inside the exposed specimens, specific mass change (Δm/S) and ranges depth of oxidation (Δd, estimated from optical microscope images such as those shown in Fig- SI-3) and reported in Table 6. The outermost and innermost profiles of the oxide layers do not have even contours. In addition, voids and delaminated regions, along with stratified sub-layers characterized by a distinct microstructure, are commonly observed. These features are signature of the detrimental effects due to the escape of volatile oxides when leaving the oxide scale, more turbulent or less, respectively, in the CCB-Cr and CCB-Nb compositions: examples are represented in Fig. 7.

A trend for the Δm/S values versus <T_H> can tentatively be identified considering the experimental net values. As a rule of thumb, CCB-Cr exhibited less propensity to form and retain solid oxides at the outer surface releasing more volatile gaseous species compared to CCB-Nb. In other words, based on the net mass change values, CCB-Nb was more resistant than CCB-Cr: for instance, CCB-Cr-E (Δm/S=1.3 mg/cm^2) exhibited more severe overall degradation compared to CCB-Nb-E (Δm/S=-3.1 mg/cm^2). The Δm/S values, more than Δd, were more representative of the final degradation. In fact, an obvious trend connecting Δd versus <T_H> was not explicity found. In any case, considering the increasing severity of the testing conditions, it was observed that the resulting thicknesses of the oxide scales remained rather limited at less than 100 μm. To corroborate the qualitative intensity of the gas release vs. temperature, plan view SEM images of the oxide scales formed in the hot zone region of all the pellets are presented in Fig. SI-4.

5. Discussion

Sub-Sections 4.1–4.2–4.3 illustrated the experimental results necessary to describe why and how the composition dependence affects the oxidation resistance of the tested CCBs. Starting from the ΔM/S vs Δd measurements, CCB-Nb and CCB-Cr withstood these testing conditions without significant degradation. On one hand, the specific mass changes (see Table 6) remained between +2.9 mg/cm^2 and −3.1 mg/cm^2, and the resulting scales thicknesses did not exceed 110 μm. To

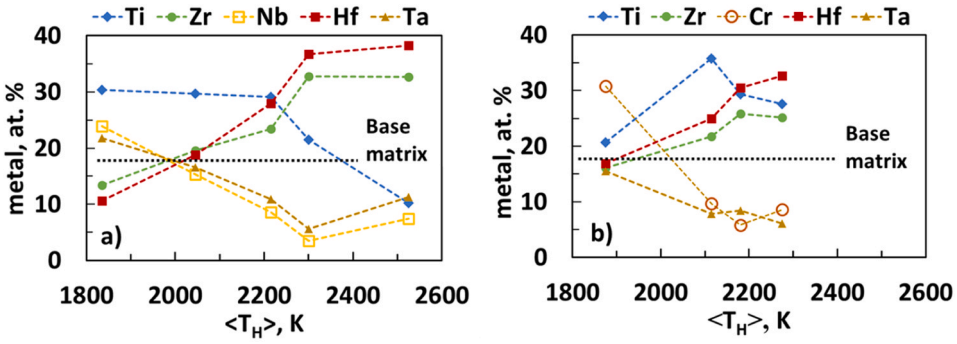

Fig. 6. ED-XRF quantitative elemental composition (on metal basis) versus average temperature <T_H> from the oxidized surfaces of CCB-Nb (left-hand panel) and CCB-Cr (right-hand panel) discs. The equiatomic reference composition of the "base matrix" is indicated.

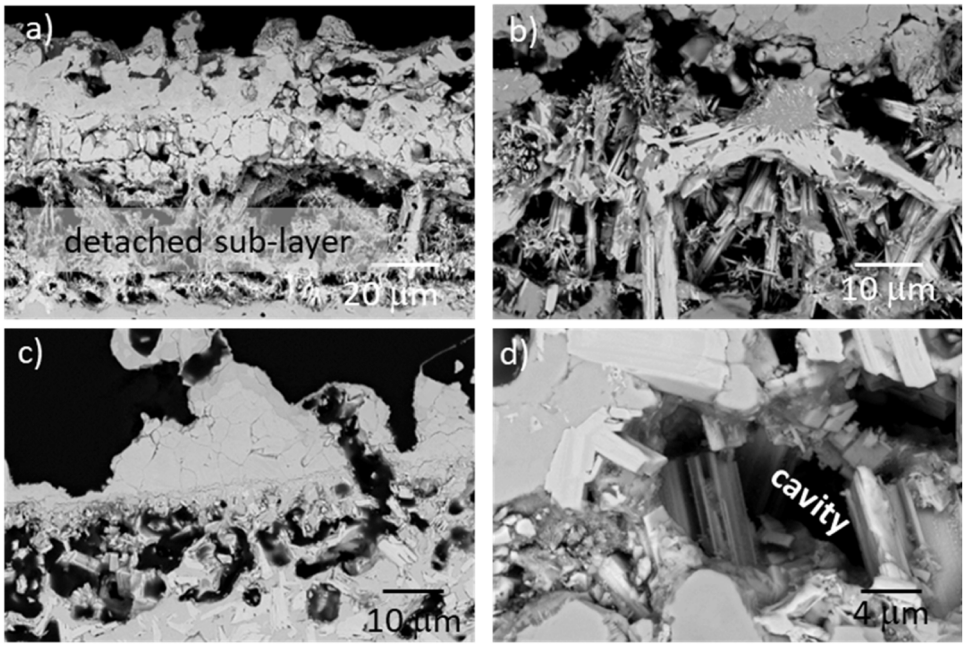

Fig. 7. Back-scattered electrons FESEM images (polished section) from the as-exposed CCB-Cr-B (a, b) and CC-Nb-B (c, d). Micrograph b) and d) are zoom inside the inner sub-layer where vapor pressures built up massively. Detached regions with cavities are indicated in a) and d).

further corroborate the assertion that CCB-Nb and CCB-Cr suffered only limited degradation, the critical analysis published by Bianco [45] of the parameters affecting the oxidation behaviour of pure and non-Si-containing ultra-high temperature diboride ceramics is useful. In fact, no examples of samples with oxide thickness below 100 μm after testing above 2273 K were found by Bianco and coworkers. In the current case, if CCB-Nb-C and CCB-Cr-C are compared, the second suffered a more severe degradation because the overall net mass change was negative. Although CCB-Nb-C and CCB-Cr-C reached comparable $<T_H>$ (i.e., 2215 K versus 2180 K), the Δd value of CCB-Nb-C was larger than that of CCB-Cr-C very likely because the detrimental effects caused by the outgassing of volatile products was greatly limited so that CCB-Nb-C could protect itself more effectively. Analogous reasoning can be applied to the comparison between CCB-Nb-D and CCB-Cr-D. However, comparing CCB-Nb-E and CCB-Cr-E, though they were exposed to the same (nominal) h_i of 5.2 MW/m^2, they reached different $<T_H>$. With such a difference in temperature noted between CCB-Nb-E and CCB-Cr-E (which may be governed by the response of the materials to the solar flux), part of the difference may be due to the extrinsic factor of a greenish deposit on the internal walls of the quartz tube during testing. On the other hand, these ceramics are brittle, especially CCB-Cr, which failed due to thermal shock during the cooling segment. The failure of the disc (see Fig. 4) precluded the completion of the ED-XRF chemical analysis (not plotted in Fig. 6).

The discrepancy between ρ_{EXP} and ρ_B (see Table 4) was attributed to the retention of unreacted B_4C in both materials. The unreacted boron carbide inclusions, especially the largest ones, are expected to act as weak spots for the overall resistance to oxidation because the dissociated air plasma would react preferentially with these areas that lack the ability to form a refractory scale. However, the content of the residual boron carbide is similar between CCB-Nb and CCB-Cr, so the same impact on the overall resistance should be similar. The thermodynamic calculations that led to the Q^{Me} descriptor (see Fig. 1) and the total vapor pressure p_{vap}^{Me} (see Fig. 2) indicates that the Cr-containing oxides have lower stability compared to Nb-containing ones. Values of Q^{Me} tending to 1, together with p_{vap}^{Me} closer to the external pressure p_0, favor the release of gaseous species and the consequent formation of porous intermediate layers in the scale for CCB-Cr. The vapor pressures of volatile Cr-containing species and their accompanying escape from the scales produce porosity in the scale as shown in the images in Fig. 7. As $<T_H>$ rises over 2000 K, the oxidized scales produced on the CCBs become more complex due to the presence of five transition metals in the compositions, each in significant amount. An example of the chemical redistribution of the starting metals is provided by FESEM-EDS analyses like that shown in Fig. 8 and Fig. 9. As supported by the calculated values of Fig. 2 (p_{O2}=1 Pa) that are farthest away from 1 Pa, the more stable solid phases are the Hf oxides, followed by Zr, Nb and Ta oxides, which are present at the internal interface between the scale and the CCB. The stable oxides form columnar shaped grains, and a Ti-depleted region forms at the scale-CCB interface (Fig. 9).

As a rule of thumb, the increase of $<T_H>$ at the exterior (i.e., p_{O2}=200 Pa) promotes the predominance of the most stable Hf-Zr-Ti based mixed oxide. Based on the quantitative determination of the metals shown in Fig. 6, the elemental composition (metal basis) of the main constituents in CCB-Nb-E are Hf =38.2 at% and Zr = 32.7 at%. A compelling feature of the outer layers of the mixed oxides, compared to the grains underneath (Fig. 10), is the presence of a phase with a molten-like appearance that may protect the underlying substrate. More details are depicted in Figures SI-5/6 to provide a deeper insight of the outer protective barrier as well as of the underlying oxidation-affected sub-layers.

By looking at phase relations in the TiO_2-ZrO_2 [46] and TiO_2-HfO_2 [47] systems, where the addition of TiO_2 to MeO_2 (Me= Zr or Hf) reduces the melting point of the TiO_2-MeO_2 system, it is conceivable that unvolatilized Ti oxide acted as a flux for the predominant Hf-Zr mixed oxides. The FESEM-EDS quantitative analyses of the scale on CC-UHTC-Nb-E determined that the outer scale contains 43 at% Hf, 36 at% Zr, 15 at% Ti, 5 at% Ta+Nb. The amount of Ti differs from that of Fig. 6 because the ED-XRF signal was collected from the entire surface, and not just from the hottest area. The role of Ti as a eutectic forming agent among the *in-situ* interacting metal oxides vs. the operating service conditions and its potential protective mechanism without extrinsic glass-forming could have profound implications which are discussed in sub-Section 5.1.

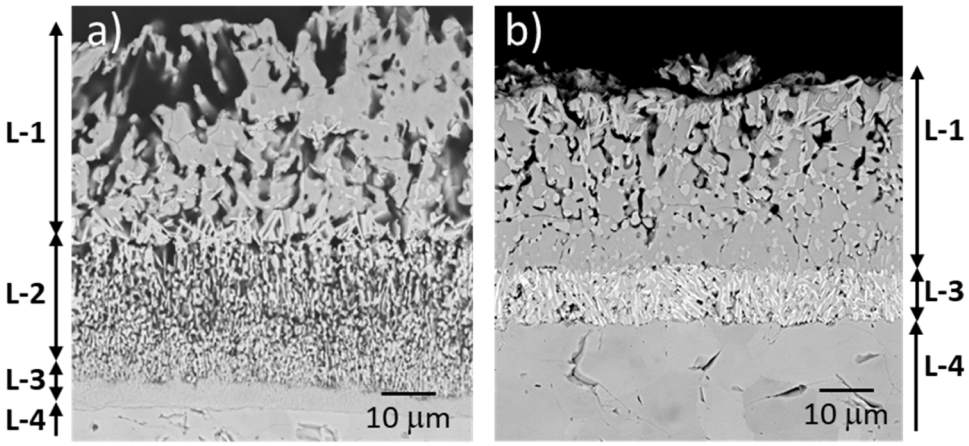

Fig. 8. Back-scattered electrons FESEM images (polished section) from the as-exposed CCB-Nb-A (a) and CCB-Nb-D (b): evolution of the inner sub-layers. Layer L-2 is supposed to merge into L-1, L-4 is the diboride unaffected matrix. Sub-layers L-2 and L-3 (a), and sub-layer L-3 (b) are examples of stratified sub-scales mentioned in the main text.

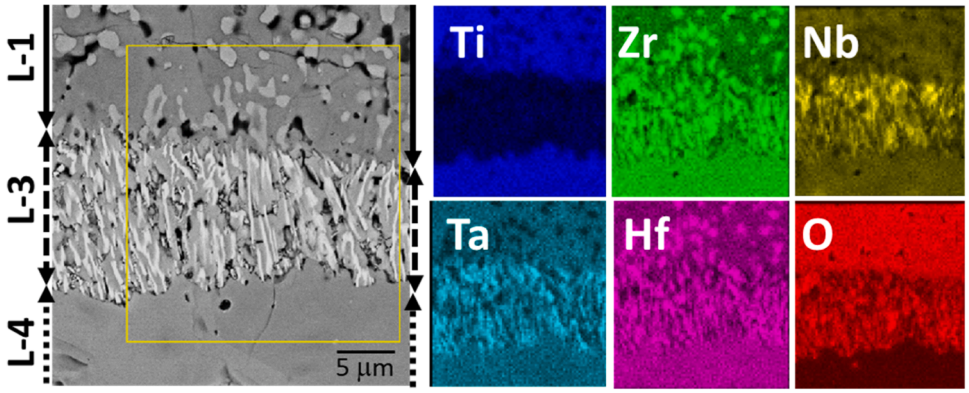

Fig. 9. CCB-Nb-D: back-scattered electrons FESEM image from the L-1/L-3/L-4 oxide/diboride interfaces and elemental FESEM-EDS mapping from the yellow box. Note the uniform intensities from the CC diboride matrix L-4.

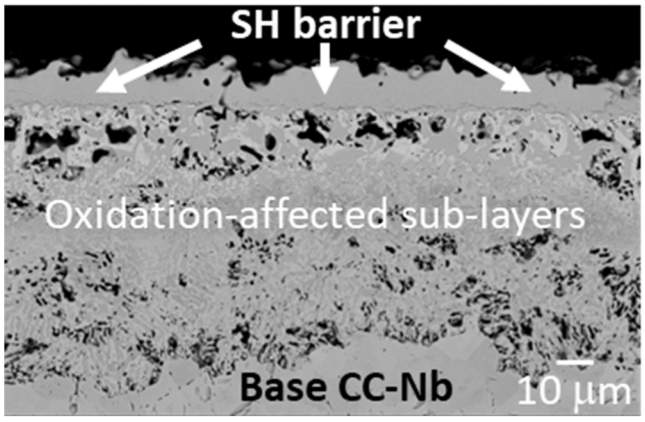

Fig. 10. Back-scattered electrons FESEM image (polished cross-section) from the oxidation-affected sub-layers underlying the outer protective (SH) oxide barrier in the as-exposed CCB-Nb-E.

5.1. Issues, outlook, and perspectives

Can CC diboride solid solutions (SSs) actually be one of the technological solutions long sought to operate in and withstand harsh conditions such as exposures to heat fluxes as high as ~5 MW/m^2 in dissociated oxygen? This emergent class of materials is gaining popularity [6,13,30,31,32,33,34,48,49,50] but remains in the early stages of research. The works of Gild [13], Feltrin [30] and Bin Hoque [31] stated that the CC diboride SSs appeared to resist oxidation better than individual MeB_2 compounds. Bin Hoque's work [31] showed that ZrB_2 and (Hf,Nb,Ta,Ti,Zr)B_2 have nearly identical ablation resistance, which suggests that dense CCBs may be strongly competing materials for structural applications where separate metal diborides have previously been studied. For the highest thermal inputs, MeB_2 ceramics containing one only metal are well documented to lack protective layers when used alone [45]. In the past, Si-containing additives like SiC [51,52] or other silicides [53] have been used to promote formation of protective glassy layers under less severe conditions (i.e., temperatures below 1923 K and neutral or oxidizing atmospheres). Two decades of experimental studies and technological advancements have explored how to get the best performance from the incorporation of SiC (particulate, whiskers or chopped fibres) into diboride matrices [54–56] or update models to better describe the oxidation kinetics of SiC-containing refractory diborides [57]. A troublesome issue that remains, which is that temperatures above 1923 K and the presence of reduced pressures result in active oxidation of SiC. Looking at the Q^{Si} data in Fig. 1, SiC (and the same is true for other silica forming agents) actively oxidizes at elevated temperatures. SiC is not removed instantaneously or completely. Only the fraction of SiC that experiences the unfavorable temperature-pressure conditions actively oxidizes while SiC in the bulk is likely retained. However, the search for improved materials led to the testing of CCBs for severe environments. Both CCB-Nb and CCB-Cr

survived the tests described herein. From the two CCBs, CCB-Nb exhibits a greater potential compared to CCB-Cr and, very likely, to other CCBs containing Mo, W or V due to the lower vapor pressures of the corresponding oxide species and the consequent capacity to retain condensed mixed oxides which provide protection against oxidation. This is supported by the thermodynamic assessment presented in Fig. 1. Similar to Cr, the Q^{Me} descriptors for Mo, W and V raises a concern about not only the phases formed during the initial stages of oxidation, but also the capability of retaining these oxides in the resulting external oxide scale.

The effects of the temperature range of eutectics among the multiple oxides that form when CCBs oxidize and directly interact with the working atmosphere are remarkable and may bring strong implications for the design of oxidation resistant CCBs. It stands to reason that, depending on the viscosity of the *in-situ* formed oxide scale, it may give rise to scenarios of increasing level of criticality: i) superior ablation resistance compared to the current UHTCs, ii) severe mass loss and recession by mechanisms such as ablation or iii) catastrophic full removal of the material. For example, a recent publication by Luo et al. pointed out that the addition of Ta_2O_5 to ZrO_2-Nb_2O_5 can decrease its melting point [58] leading to an overall decrease of the ablation resistance compared to an initial CCB composition that is free of Nb and Ta. In this regard, Zeng et al., [48] tested $Zr_{0.8}Ti_{0.2}C_{0.74}B_{0.26}$ up to 3273 K and recognized a rate of material loss at 2723 K over 12 times better than conventional ZrC that was attributed to the presence of Ti as second phase which, in turn, led to the formation of (Zr,Ti)O_2. Such a layer on the surface protects the underlying sub-layers by conferring a self healing ability to the in-situ formed oxide scale. This finding can help increase the understanding of the oxidation mechanisms not only in refractory CCBs but also in refractory alloys [59], carbides [60,61], oxycarbides [62], and carbonitrides [63,64] and highlight principles to guide their design. The examples of CC carbides [60,61] tested at very high temperatures is helpful to elucidate the effect of separate metals present in the materials. In fact, Chen et al., [60] tested Nb- and Ta-doped (Hf,Ti,Zr) carbides at 2723 K in air at 20 kPa for several minutes and concluded that, compared to Nb, the retention of Ta in the oxycarbide scale slowed oxygen diffusion and, therefore, it improved the overall oxidation resistance of (Hf,Ti, Zr) carbide. The key role of Ta was confirmed by Lv et al., when they found a proper (non-equiatomic) amount of Ta in multicomponent $(Hf_{0.4}Zr_{0.4}Ta_{0.2})B_2$ coatings for C/C composites to enable superior ablation resistance compared to diboride-modified Si-based coatings [65]. The same authors exacerbated the testing envelope of the (Hf,Ti,Ta,Zr)C material applying more severe conditions up to 2873 K in a fast-flying gas using a plasma gun [61]: in this case, the surface temperature of the sample exceeded the melting point of Ti- and Ta-rich oxides which were completely removed and led to full disintegration of the sample. The evidence of such an experiment emphasizes how the design of the composition grouping of the CC materials, i.e., the assemblage of diverse metals coming from IV, V and VI group, is vital in determining their *survivability in a specific operating envelope*. Even multi-component materials such as CCB-Nb or CCB-Cr do not escape the limitations imposed by the instability of low-melting point oxides as well as by the preferential depletion of the starting constituents: they are collateral effects that must be accepted, managed, and possibly mitigated. According to the thermodynamic favorability of the respective oxides as described in Fig. 1, a guiding principle to design the oxidation resistance of the CCBs seems to arise from the presence of both Zr and Hf. In fact, the Hf-Zr rich oxide is stable, which provides resistance to oxidation compared to the individual MeB_2 compounds alone. The formation of a more complex oxide scale may promote superior resistance to degradation as shown by the Hf-Zr-Ti mixed oxide that formed on CCB-Nb-E. For a temperature range up to 2500 K in quasi-static interacting atmosphere, the presence of Ti appeared to act as a "glass-like promoter", enabling the "*in-situ*" formed scale to be capable of sealing the surface by resisting the tendency to fully volatilize. Also, the introduction of V group metals may contribute to adjusting the viscosity of the melt spreading out the exposed surface. The success of this approach should be supported by robust thermodynamic tools. The database of multi-element phase diagrams is lacking, which means that testing campaigns are needed to generate data to partially address this lack of understanding.

Optimizing the metal concentrations in the CCB formulation by deviating from an equiatomic composition may bring unexpected advantages [49]. Preferential oxidation may initiate partial depletion of some components of the CCB that could lead to the loss of integrity and other properties of the underlying material. In this regard, changing the starting metal composition to deviate from equiatomic fractions may eliminate the benefit achieved by maximizing the configurational entropy, ΔS^{C}_{mix}. On the other hand, developing materials with improved oxidation/ablation resistance may offset the loss of configurational entropy. In fact, if a CCB is stabilized by configurational entropy, it is rather obvious that preferential oxidation occurring in an oxidizing environment will deplete the substrate of one or more constituents (Hf and Zr in the present case) and de-stabilizes the solid solution. It follows that the advantage coming from the configurational entropy in stabilizing the solid solution is somehow impaired due to the large negative free energies of the oxidation reactions, especially those of the IV group metal oxides (see Fig. SI-7). Nevertheless, the expansion of compositional space may still be pursued. The thermodynamic calculations of the present work provide guidance in compositional design, minimizing the concentration of those metals with Q^{Me} values above ~3 %: the choice of such a threshold value is merely justified by the calculated Q^{Me} values at 2200 K for Cr (11.4 %), Nb (9.6 %), Ta (2.8 %) and Ti (0.6 %) since we observed that a temperature of 2200 K demarcates the upper limit of operating range where mass volatilization started increasing significantly. The minimization of the metal concentration in the final CCB can be relaxed towards the equiatomicity of the metallic end members of the solid solution, if the projected operating temperature lies below 2200 K.

To conclude, the model presented and discussed herein showed useful guiding principles for design of CCB even though it did not consider any interactions among the constituent metals and assumed the worst case scenario for maximum possible volatilization. Improvements in the thermodymanic database are necessary to refine the model and the ability to design compositions with favorable stability and oxidation resistance.

6. Conclusions

The evolution of the oxidation reactions in two (nominally equimolar) compositionally complex diboride solid solutions was determined during exposure in dissociated air plasma with surface temperatures in the range of 1800 K to 2500 K. The materials withstood the severe testing condition with small overall mass changes. Composition and compactness of the oxide scales that grew in-situ depended on the initial combination of metals in the CCB. The presence of Zr and Hf favored the formation of a stable external oxide layer, while Nb, Ta and Ti, in this order, had increasing tendencies to volatilize as temperature increased. Cr was not appropriate as a base constituent of the starting solid solution because the Cr-containing species were volatile. A thermodynamic assessment predicted: i) the selective tendency of various metals to interact with oxygen and volatilize; and ii) the influence of the equilibrium oxygen partial pressure for the metal and its oxide to set conditions that lead to sub-layers depleted of certain metals, like Ti. Protective mechanisms were active up to 2500 K. For higher temperature, the material degradation will still be affected by the choice among IV, V, or VI group metals.

Declaration of Competing Interest

The authors declare that they have no known competing financial

interests or personal relationships that could have appeared to influence the work reported in this paper.

Acknowledgements

The authors are grateful to PROMES-CNRS for providing beamtime in the Odeillo solar furnace (Font-Romeu-Odeillo-Via, France). The effort of W. Fahrenholtz and G. Hilmas was supported by the U.S. National Science Foundation through grant CMMI-1902069 and through the Office of Naval Research on a Multidisciplinary University Research Initiative (MURI) program under project number N00014–21–1–2515. The authors also thank Lun Feng (Missouri University of Science and Technology) and Federico Saraga (ISSMC-CNR) for the preparation, respectively, of the as-sintered pellets and of the post -test polished cross-sections.

Appendix A. Supporting information

Supplementary data associated with this article can be found in the online version at doi:10.1016/j.jeurceramsoc.2024.116963.

References

[1] K.O. Shvydyuk, J. Nunes-Pereira, F.F. Rodrigues, A.P. Silva, Review of ceramic composites in aeronautics and aerospace: a multifunctional approach for TPS, TBC and DBD applications, Ceramics 6 (1) (2023) 195–230, https://doi.org/10.3390/ceramics6010012.

[2] S. Tang, C. Hu, Design, preparation and properties of carbon fiber reinforced ultra-high temperature ceramic composites for aerospace applications: a review, J. Mater. Sci. Technol. 33 (2) (2017) 117–130, https://doi.org/10.1016/j.jmst.2016.08.004.

[3] S. Jones, Advanced manufacturing applied to nuclear fusion—challenges and solutions, J. Phys.: Energy 5 (4) (2023) 042001, https://doi.org/10.1088/2515-7655/acf687.

[4] R.K. Poobalan, H.C. Barshilia, B. Basu, Recent trends and challenges in developing boride and carbide-based solar absorbers for concentrated solar power, Sol. Energy Mater. Sol. Cells 245 (2022) 111876, https://doi.org/10.1016/j.solmat.2022.111876.

[5] K.A. Kane, B.A. Pint, D. Mitchell, J.A. Haynes, Oxidation of ultrahigh temperature ceramics: kinetics, mechanisms, and applications, J. Eur. Ceram. Soc. 41 (13) (2021) 6130–6150, https://doi.org/10.1016/j.jeurceramsoc.2021.05.055.

[6] A.B. Peters, D. Zhang, S. Chen, et al., Materials design for hypersonics, Nat. Commun. 15 (1) (2024) 3328, https://doi.org/10.1038/s41467-024-46753-3.

[7] Z.-Y. Wei, G.-H. Meng, L. Chen, et al., Progress in ceramic materials and structure design toward advanced thermal barrier coatings, J. Adv. Ceram. 11 (7) (2022) 985–1068, https://doi.org/10.1007/s40145-022-0581-7.

[8] C. Pellegrini, M. Balat-Pichelin, O. Rapaud, E. Bêche, Oxidation resistance of Zr- and Hf-diboride composites containing SiC in air plasma up to 2600 K for aerospace applications, Ceram. Int 48 (2) (2022) 2177–2190, https://doi.org/10.1016/j.ceramint.2021.09.310.

[9] C. Pellegrini, M. Balat-Pichelin, O. Rapaud, E. Bêche, Oxidation resistance and emissivity of diboride-based composites containing tantalum disilicide in air plasma up to 2600 K for space applications, Ceram. Int 48 (19) (2022) 27878–27890, https://doi.org/10.1016/j.ceramint.2022.06.090.

[10] C. Pellegrini, M. Balat-Pichelin, O. Rapaud, E. Bêche, Y. Thébault, Oxidation resistance up to 2600 K under air plasma of (Zr/Hf)B2 composites containing 20 vol% AlN for hypersonic applications, Ceram. Int 49 (19) (2023) 31634–31648, https://doi.org/10.1016/j.ceramint.2023.07.117.

[11] L. Feng, W.G. Fahrenholtz, D.W. Brenner, High-entropy ultra-high-temperature borides and carbides: a new class of materials for extreme environments, Annu Rev. Mater. Res 51 (1) (2021) 165–185, https://doi.org/10.1146/annurev-matsci-080819-121217.

[12] A.J. Wright, J. Luo, A step forward from high-entropy ceramics to compositionally complex ceramics: a new perspective, J. Mater. Sci. 55 (23) (2020) 9812–9827, https://doi.org/10.1007/s10853-020-04583-w.

[13] J. Gild, Y. Zhang, T. Harrington, et al., High-entropy metal diborides: a new class of high-entropy materials and a new type of ultrahigh temperature ceramics, Sci. Rep. 6 (1) (2016) 37946, https://doi.org/10.1038/srep37946.

[14] C.M. Rost, E. Sachet, T. Borman, et al., Entropy-stabilized oxides, Nat. Commun. 6 (1) (2015) 8485, https://doi.org/10.1038/ncomms9485.

[15] B.L. Musicó, D. Gilbert, T.Z. Ward, et al., The emergent field of high entropy oxides: Design, prospects, challenges, and opportunities for tailoring material properties, APL Mater. 8 (4) (2020) 040912, https://doi.org/10.1063/5.0003149.

[16] G. Akopov, L.E. Pangilinan, R. Mohammadi, R.B. Kaner, Perspective: superhard metal borides: a look forward, APL Mater. 6 (7) (2018) 070901, https://doi.org/10.1063/1.5040763.

[17] F. Wang, F. Monteverde, B. Cui, Will high-entropy carbides and borides be enabling materials for extreme environments? Int. J. Extrem. Manuf. 5 (2) (2023) 022002 https://doi.org/10.1088/2631-7990/acbd6e.

[18] M. Gaboardi, F. Monteverde, F. Saraga, et al., Local structure in high-entropy transition metal diborides, Acta Mater. 239 (2022) 118294, https://doi.org/10.1016/j.actamat.2022.118294.

[19] Z. Wang, Z.-T. Li, S.-J. Zhao, Z.-G. Wu, High-entropy carbide ceramics: a perspective review, Tungsten 3 (2) (2021) 131–142, https://doi.org/10.1007/s42864-021-00085-7.

[20] R.-Z. Zhang, M.J. Reece, Review of high entropy ceramics: design, synthesis, structure and properties, J. Mater. Chem. A Mater. 7 (39) (2019) 22148–22162, https://doi.org/10.1039/C9TA05698J.

[21] H. Xiang, Y. Xing, F. Dai, et al., High-entropy ceramics: present status, challenges, and a look forward, J. Adv. Ceram. 10 (3) (2021) 385–441, https://doi.org/10.1007/s40145-021-0477-y.

[22] O.F. Dippo, N. Mesgarzadeh, T.J. Harrington, G.D. Schrader, K.S. Vecchio, Bulk high-entropy nitrides and carbonitrides, Sci. Rep. 10 (1) (2020) 21288, https://doi.org/10.1038/s41598-020-78175-8.

[23] A. Salian, P. Sengupta, I. Vishalakshi Aswath, A. Gowda, S. Mandal, A review on high entropy silicides and silicates: Fundamental aspects, synthesis, properties, Int. J. Appl. Ceram. Technol. 20 (5) (2023) 2635–2660, https://doi.org/10.1111/ijac.14422.

[24] F. Monteverde, M. Gaboardi, F. Saraga, L. Feng, W. Fahrenholtz, G. Hilmas, Anisotropic thermal expansion in high-entropy multicomponent AlB_2 -type diboride solid solutions, Int. J. Extrem. Manuf. 5 (1) (2023) 015505, https://doi.org/10.1088/2631-7990/acabee.

[25] L. Feng, W.G. Fahrenholtz, G.E. Hilmas, S. Curtarolo, Boro/carbothermal reduction co-synthesis of dual-phase high-entropy boride-carbide ceramics, J. Eur. Ceram. Soc. 43 (6) (2023) 2708–2712, https://doi.org/10.1016/j.jeurceramsoc.2022.12.056.

[26] N. Ni, Q. Ding, Y. Shi, et al., Ablation behavior of high-entropy carbides ceramics (Hf0.2Zr0.2Ta0.2Nb0.2Ti0.2)C upon exposition to an oxyacetylene torch at 2000 °C, J. Eur. Ceram. Soc. 43 (6) (2023) 2306–2319, https://doi.org/10.1016/j.jeurceramsoc.2023.01.017.

[27] Y. Wang, B. Zhang, C. Zhang, J. Yin, M.J. Reece, Ablation behaviour of (Hf-Ta-Zr-Nb)C high entropy carbide ceramic at temperatures above 2100 °C, J. Mater. Sci. Technol. 113 (2022) 40–47, https://doi.org/10.1016/j.jmst.2021.09.064.

[28] J. Li, Y. Zhang, Y. Zhao, Y. Zou, J. Lv, J. Li, A novel (Hf1/3Zr1/3Ti1/3)C medium-entropy carbide coating with excellent long-life ablation resistance applied above 2100 °C, Compos B Eng. 251 (2023) 110467, https://doi.org/10.1016/j.compositesb.2022.110467.

[29] Z. Wen, Y. Liu, H. Yu, S. Jiang, Y. Qin, Y. Chu, Sm-composition engineering of (Hf, Zr, Ta, Sm)B2 high-entropy diborides for superior oxidation resistance, Corros. Sci. 227 (2024) 111753, https://doi.org/10.1016/j.corsci.2023.111753.

[30] A.C. Feltrin, F. Akhtar, High-temperature oxidation kinetics of a metastable dual-phase diboride and a high-entropy diboride, J. Eur. Ceram. Soc. 43 (16) (2023) 7363–7372, https://doi.org/10.1016/j.jeurceramsoc.2023.08.001.

[31] M.S.Bin Hoque, M. Milich, M.S. Akhanda, et al., Thermal and ablation properties of a high-entropy metal diboride: $(Hf_{0.2}Zr_{0.2}Ti_{0.2}Ta_{0.2}Nb_{0.2})B_2$, J. Eur. Ceram. Soc. 43 (11) (2023) 4581–4587, https://doi.org/10.1016/j.jeurceramsoc.2023.03.065.

[32] L. Backman, J. Gild, J. Luo, E.J. Opila, Part I: Theoretical predictions of preferential oxidation in refractory high entropy materials, Acta Mater. 197 (2020) 20–27, https://doi.org/10.1016/j.actamat.2020.07.003.

[33] L. Backman, J. Gild, J. Luo, E.J. Opila, Part II: Experimental verification of computationally predicted preferential oxidation of refractory high entropy ultra-high temperature ceramics, Acta Mater. 197 (2020) 81–90, https://doi.org/10.1016/j.actamat.2020.07.004.

[34] L. Backman, J. Gild, M. Qin, J. Luo, E.J. Opila, Composition dependence of oxidation resistance in high entropy ultra-high temperature ceramics, Open Ceram. (2024) 100563, https://doi.org/10.1016/j.oceram.2024.100563.

[35] L. Backman, B.M. Hunter, M.L. Weaver, E.J. Opila, Invited Article: The oxidation kinetics and mechanisms observed during ultra-high temperature oxidation of (HfZrTiTaNb)C and (HfZrTiTaNb)B2, J. Appl. Phys. 136 (5) (2024), https://doi.org/10.1063/5.0206227.

[36] Z. Ye, Y. Zeng, X. Xiong, Q. Wen, H. Lun, Elucidating the role of preferential oxidation during ablation: Insights on the design and optimization of multicomponent ultra-high temperature ceramics, J. Adv. Ceram. 11 (12) (2022) 1956–1975, https://doi.org/10.1007/s40145-022-0659-2.

[37] L. Feng, F. Monteverde, W.G. Fahrenholtz, G.E. Hilmas, Superhard high-entropy AlB2-type diboride ceramics, Scr. Mater. 199 (2021) 113855, https://doi.org/10.1016/j.scriptamat.2021.113855.

[38] M. Balat-Pichelin, A. Vesel, Neutral oxygen atom density in the MESOX air plasma solar furnace facility, Chem. Phys. 327 (1) (2006) 112–118, https://doi.org/10.1016/j.chemphys.2006.03.034.

[39] A.Roine. HSC version 6.12. n.d.

[40] A. Hoseinpur, S. Andersson, K. Tang, J. Safarian, Selective vacuum evaporation by the control of the chemistry of gas phase in vacuum refining of Si, Langmuir 37 (24) (2021) 7473–7485, https://doi.org/10.1021/acs.langmuir.1c00876.

[41] D. Wang, Y. Zeng, X. Xiong, et al., Ablation behavior of ZrB2–SiC protective coating for carbon/carbon composites, Ceram. Int. 41 (6) (2015) 7677–7686, https://doi.org/10.1016/j.ceramint.2015.02.096.

[42] E.J. Opila, R.E. Hann, Paralinear oxidation of CVD SiC in water vapor, J. Am. Ceram. Soc. 80 (1) (1997) 197–205, https://doi.org/10.1111/j.1151-2916.1997.tb02810.x.

[43] S.J. McCormack, K. Tseng, R.J.K. Weber, et al., In-situ determination of the HfO_2–Ta_2O_5 -temperature phase diagram up to 3000°C, J. Am. Ceram. Soc. 102 (8) (2019) 4848–4861, https://doi.org/10.1111/jace.16271.

[44] Q. Liu, X. Hu, W. Zhu, J. Guo, Z. Tan, Effects of Ta_2O_5 content on mechanical properties and high-temperature performance of $Zr_6Ta_2O_{17}$ thermal barrier

coatings, J. Am. Ceram. Soc. 104 (12) (2021) 6533–6544, https://doi.org/10.1111/jace.17990.
[45] G. Bianco, A. Nisar, C. Zhang, B. Boesl, A. Agarwal, A critical analysis of the parameters affecting the oxidation behavior of ultra-high-temperature diboride ceramics, J. Am. Ceram. Soc. 105 (3) (2022) 1939–1953, https://doi.org/10.1111/jace.18218.
[46] T. Noguchi, M. Mizuno, Phase Changes in the ZrO_2 -TiO_2 system, Bull. Chem. Soc. Jpn 41 (12) (1968) 2895–2899, https://doi.org/10.1246/bcsj.41.2895.
[47] R. RUH, G.W. Hollenberg, E.G. Charles, V.A. Patel, Phase relations and thermal expansion in the system HfO_2 -TiO_2, J. Am. Ceram. Soc. 59 (11–12) (1976) 495–499, https://doi.org/10.1111/j.1151-2916.1976.tb09416.x.
[48] Y. Zeng, D. Wang, X. Xiong, et al., Ablation-resistant carbide Zr0.8Ti0.2C0.74B0.26 for oxidizing environments up to 3,000 °C, Nat. Commun. 8 (1) (2017) 15836, https://doi.org/10.1038/ncomms15836.
[49] Z. Wen, H. Meng, S. Jiang, Z. Tang, Y. Liu, Y. Chu, Non-equimolar (Hf,Zr,Ta,W)B2 high-entropy diborides enable superior oxidation resistance, Sci. China Mater. 66 (8) (2023) 3213–3222, https://doi.org/10.1007/s40843-023-2461-y.
[50] P. Zhang, C. Cheng, B. Liu, et al., Multicomponent (Hf0.25Zr0.25Ti0.25Cr0.25)B2 ceramic modified SiC–Si composite coatings: In-situ synthesis and high-temperature oxidation behavior, Ceram. Int. 48 (9) (2022) 12608–12624, https://doi.org/10.1016/j.ceramint.2022.01.129.
[51] F. Monteverde, F. Saraga, T. Reimer, D. Sciti, Thermally stimulated self-healing capabilities of ZrB2-SiC ceramics, J. Eur. Ceram. Soc. 41 (15) (2021) 7423–7433, https://doi.org/10.1016/j.jeurceramsoc.2021.08.012.
[52] F. Monteverde, L. Scatteia, Resistance to thermal shock and to oxidation of metal diborides–SiC ceramics for aerospace application, J. Am. Ceram. Soc. 90 (4) (2007) 1130–1138, https://doi.org/10.1111/j.1551-2916.2007.01589.x.
[53] A. Nisar, R. Hassan, A. Agarwal, K. Balani, Ultra-high temperature ceramics: Aspiration to overcome challenges in thermal protection systems, Ceram. Int. 48 (7) (2022) 8852–8881, https://doi.org/10.1016/j.ceramint.2021.12.199.
[54] L.M. Rueschhoff, C.M. Carney, Z.D. Apostolov, M.K. Cinibulk, Processing of fiber-reinforced ultra-high temperature ceramic composites: a review, Int. J. Ceram. Eng. Sci. 2 (1) (2020) 22–37, https://doi.org/10.1002/ces2.10033.
[55] F. Huang, H. Wang, C. Fang, et al., Improved damage tolerance and oxidation resistance of $(Ti_{0.2}\ Zr_{0.2}\ Hf_{0.2}\ Nb_{0.2}\ Ta_{0.2})B_2$ –SiC by introducing chopped carbon fibers, J. Adv. Ceram. 13 (1) (2024) 101–112, https://doi.org/10.26599/JAC.2024.9220844.
[56] R. Guo, Z. Li, L. Li, R. Zheng, C. Ma, Oxidation behavior of high-entropy (Zr0.2Hf0.2Ta0.2Nb0.2Ti0.2)B2 ceramic with 20% SiC addition, J. Eur. Ceram. Soc. 44 (8) (2024) 5181–5189, https://doi.org/10.1016/j.jeurceramsoc.2024.02.019.
[57] P. Mogilevsky, M.K. Cinibulk, Oxidation kinetics of silicon carbide-containing refractory diborides, I: Revised model, J. Am. Ceram. Soc. (2023), https://doi.org/10.1111/jace.19471.
[58] P. Luo, X. Wu, W. Xiao, et al., Phase equilibria in the ZrO_2 –Ta_2O_5 –Nb_2O_5 system: Experimental studies and thermodynamic modeling, J. Am. Ceram. Soc. 105 (1) (2022) 668–686, https://doi.org/10.1111/jace.18079.
[59] R. Su, H. Zhang, G. Ouyang, L. Liu, D.D. Johnson, J.H. Perepezko, Oxidation mechanism in a refractory multiple-principal-element alloy at high temperature, Acta Mater. 246 (2023) 118719, https://doi.org/10.1016/j.actamat.2023.118719.
[60] S. Chen, Nb- and Ta-doped (Hf,Zr,Ti)C multicomponent carbides with enhanced oxidation resistance at 2500 °C, J. Adv. Ceram. 13 (3) (2024) 332–344. JWZCWSYZXLTLXX.
[61] S. Chen, Z. Chen, W. Song, Y. Zeng, X. Xiong, High-temperature ablation behavior and failure mechanism of (Hf0.25Zr0.25Ti0.25Ta0.25)C high-entropy carbide in wide temperature range, J. Eur. Ceram. Soc. 44 (12) (2024) 6815–6826, https://doi.org/10.1016/j.jeurceramsoc.2024.05.021.
[62] Z. Wen, Z. Tang, H. Meng, Y. Chu, A promising new class of high-entropy ceramics: High-entropy oxycarbides with good oxidation resistance, Corros. Sci. 207 (2022) 110574, https://doi.org/10.1016/j.corsci.2022.110574.
[63] Z. Peng, W. Sun, X. Xiong, H. Zhang, F. Guo, J. Li, Novel refractory high-entropy ceramics: Transition metal carbonitrides with superior ablation resistance, Corros. Sci. 184 (2021) 109359, https://doi.org/10.1016/j.corsci.2021.109359.
[64] Y. Wang, X. Wang, S. Li, M.J. Reece, Improved oxidation resistance of (Zr-Nb-Hf-Ta)(C, N) high entropy carbonitrides, Corros. Sci. 225 (2023) 111583, https://doi.org/10.1016/j.corsci.2023.111583.
[65] J. Lv, W. Li, T. Li, et al., Multicomponent (Hf-Zr-Ta)B2 coatings for carbon/carbon composites and structural optimization enabling superior ablation resistance, J. Mater. Sci. Technol. 204 (2025) 115–126, https://doi.org/10.1016/j.jmst.2024.03.050.